Adhesion of Biologically Inspired Vertical and Angled Polymer Microfiber Arrays

3 AUTHORS, INCLUDING:

Burak Aksak
Texas Tech University

25 PUBLICATIONS   **776** CITATIONS

SEE PROFILE

Metin Sitti
Max Planck Institute for Intelligent Systems, …

290 PUBLICATIONS   **7,803** CITATIONS

SEE PROFILE

Adhesion of Biologically Inspired Vertical and Angled Polymer Microfiber Arrays

Burak Aksak,[†] Michael P. Murphy,[†] and Metin Sitti*

NanoRobotics Laboratory, Department of Mechanical Engineering, Carnegie Mellon University, Pittsburgh, Pennsylvania 15213

This paper proposes an approximate adhesion model for fibrillar adhesives for developing a fibrillar adhesive design methodology and compares numerical simulation adhesion results with macroscale adhesion data from polymer microfiber array experiments. A technique for fabricating microfibers with a controlled angle is described for the first time. Polyurethane microfibers with different hardnesses, angles, and aspect ratios are fabricated using optical lithography and polymer micromolding techniques and tested with a custom tensile adhesion measurement setup. Macroscale adhesion and overall work of adhesion of the microfiber arrays are measured and compared with the models to observe the effect of fiber geometry and preload. The adhesion strength and work of adhesion behavior of short and long vertical and long angled fiber arrays have similar trends with the numerical simulations. A scheme is also proposed to aid in optimized fiber adhesive design.

1. Introduction

Fibrillar adhesives on the feet of geckos and spiders and other animals have been of great interest because they can repeatedly attach to wide range of surfaces with a controllable adhesion strength in various environments including vacuum and leave no residue. Furthermore, fibrillar adhesives are self-cleaning, which allows for long lifetime and repeated use without significant performance degradation.[11] These foot-hairs conform to the surface roughness to increase the real contact area, resulting in high adhesion by surface forces.[3] This adhesion, called dry adhesion, is argued to arise from molecular surface forces such as van der Waals forces,[3,4] possibly in combination with capillary forces.[12,26] The complexity of the structure of these fibers differs among the species of animal. For large lizards such as the *Tokay*

gecko, the fibers take on a complicated branched structure, whereas for lighter animals such as spiders and anoles, the structure is a simple array of angled high aspect ratio microfibers.[1] Some gecko species have adhesion strength capabilities as high as 100 kPa.[3] In geckos, the oriented fibers are made of a stiff biomaterial (β-keratin) with a Young's modulus of approximately 4 GPa[23] and have diameters from 0.2 to 5 μm.[1] The structure and material properties such as Young's modulus allow the fibers to individually bend and adapt to a wide variety of surface roughnesses and also to return to their original shape after release from the surface. Fabrication of similar synthetic structures would enable the production of long-lifetime reusable fibrillar adhesives with broad applications.

The enhanced adhesion from fibrillar surfaces has been studied and described in terms of fracture mechanics, elastic beam theory, and surface interaction forces,[6,7,10,13,22,23,27] including analysis of the effects of tip shape and fiber size.[2,8] Work has also been

* Corresponding author. sitti@cmu.edu.
† Equally contributing co-first authors.

(1) Arzt, E.; Gorb, S.; Spolenak, R. From micro to nano contacts in biological attachment devices. *Proc. Natl. Acad. Sci. U.S.A.* **2003,** *100* (19), 10603–06.
(2) Spolenak, R.; Gorb, S.; Gao, H.; Arzt, E. Effects of contact shape on the scaling of biological attachments. *Proc. R. Soc. London, Ser. A* **2005,** *461,* 305–319.
(3) Autumn, K.; Liang, Y. A.; Hsieh, S. T.; Zesch, W.; Chan, W. P.; Kenny, T. W.; Fearing, R.; Full, R. J. Adhesive force of a single gecko foot-hair. *Nature (London)* **2000,** *405,* 681–685.
(4) Autumn, K.; Sitti, M.; Liang, Y. A.; Peattie, A. M.; Hansen, W. R.; Sponberg, S.; Kenny, T. W.; Fearing, R.; Israelachvili, J. N.; Full, R. J. Evidence for van der waals adhesion in gecko setae. *Proc. Natl. Acad. Sci. U.S.A.* **2002,** *99,* 12252–56.
(5) Bogdanov, A. L.; Peredkov, S. S. Use of su-8 pr for very high aspect ratio x-ray lithography. *Microelectron. Eng.* **2000,** *53,* 493–496.
(6) Chung, J. Y.; Chaudhury, M. K. Roles of discontinuities in bio-inspired adhesive pads. *J. R. Soc. Interface* **2005,** *2,* 55–61.
(7) Crosby, A.; Hageman, M.; Duncan, A. Controlling polymer adhesion with "pancakes". *Langmuir* **2005,** *21,* 11738–11743.
(8) Gao, H.; Yao, H. Shape insensitive optimal adhesion of nanoscale fibrillar structures. *Proc. Natl. Acad. Sci. U.S.A.* **2004,** *101* (21), 7851–7856.
(9) Geim, A. K.; Dubonos, S. V.; Grigorieva, I. V.; Novoselov, K. S.; Zhukov, A. A.; Shapoval, S. Y. Microfabricated adhesive mimicking gecko foot-hair. *Nat. Mater.* **2003,** *2,* 461–463.
(10) Glassmaker, N. J.; Jagota, A.; Hui, C. Y.; Kim, J. Design of biomimetic fibrillar interfaces: 1. making contact. *J. R. Soc. Interface* **2004,** *1* (1), 23–33.
(11) Hansen, W.; Autumn, K. Evidence for self-cleaning in gecko setae. *Proc. Natl. Acad. Sci. U.S.A.* **2005,** *102,* 385–389.
(12) Huber, G.; Mantz, H.; Spolenak, R.; Mecke, K.; Jacobs, K.; Gorb, S. N.; Arzt, E. Evidence for capillarity contributions to gecko adhesion from single spatula nanomechanical measurements. *Proc. Natl. Acad. Sci. U.S.A.* **2005,** *102,* 16293–16296.
(13) Hui, C.; Glassmaker, N. J.; Tang, T.; Jagota, A. Design of biomimetic fibrillar interfaces: 2. mechanics of enhanced adhesion. *J. R. Soc. Interface* **2004,** *1,* 35–48.

(14) Hung, K.-Y.; Hu, H.-T.; Tseng, F.-G. Application of 3d glycerol-compensated inclined-exposure technology to an integrated optical pick-up head. *J. Micromech. Microeng.* **2004,** *14,* 975–983.
(15) Israelachvili, J. *Intermolecular and Surface Forces*; Academic Press: London, 1992.
(16) Johnson, K. L.; Kendall, K.; Roberts, A. D. Surface energy and contact of elastic solids. *Proc. R. Soc. London, Ser. A* **1971,** *324,* 301–313.
(17) Majidi, C.; Groff, R.; Fearing, R. Clumping and packing of hair arrays manufactured by nanocasting. *Proc. ASME Int. Mech. Eng. Congress Exposition* **2004,** 579–584.
(18) Maugis, D. Adhesion of spheres: the JKR-DMT transition using a dugdale model. *J. Colloid Interface Sci.* **1992,** *150,* 243–269.
(19) Maugis, D.; Cardona, M.; Fulde, P.; von Klitzing, K.; Merlin, R.; Queisser, H.; Stormer, H. *Contact, Adhesion and Rupture of Elastic Solids*; Springer: Berlin, 2000.
(20) Menon, C.; Murphy, M.; Sitti, M. Gecko inspired surface climbing robots. *Proc. IEEE Int. Conf. Robotics Biomimetics* **2004,** 431–436.
(21) Northen, M. T.; Turner, K. L. A batch fabricated biomimetic dry adhesive. *Nanotechnology* **2005,** *16,* 1159–1166.
(22) Perrson, B. N. J.; Gorb, S. The effect of surface roughness on the adhesion of elastic plates with application to biological systems. *J. Chem. Phys.* **2003,** *119* (21), 11437–11444.
(23) Persson, B. N. J. On the mechanism of adhesion in biological systems. *J. Chem. Phys.* **2003,** *118,* 7614–7621.
(24) Shew, R.-Y.; Hung, J.-T.; Huang, T.-Y.; Liu, K.-P.; Chou, C.-P. High resolution x-ray micromachining using su-8 resist. *J. Micromech. Microeng.* **2003,** *13,* 708–713.
(25) Sitti, M.; Fearing, R. Synthetic gecko foot-hair micro/nanostructures as dry adhesives. *J. Adhes. Sci. Technol.* **2003,** *17* (5), 1055–74.
(26) Sun, W.; Neuzil, P.; Kustandi, T.; Oh, S.; Samper, V. D. The nature of the gecko lizard adhesive force. *Biophys. J. Biophys. Lett.* **2005,** L14–L17.

conducted to create synthetic fiber adhesives via various fabrication techniques. Since van der Waals forces are universal, a wide variety of materials and techniques may be used to construct the fibers. Methods such as electron-beam lithography,[9] micro/nanomolding,[10,17,20,25] and self-assembly are employed to fabricate fibers from polymers,[4,25] polymer organorods,[21] and multiwalled carbon nanotubes.[28,29]

Whereas previous works focus mainly on theoretical either modeling or fabrication and testing of fibrillar interfaces only, this work aims to propose theoretical approximate fibrillar interface models which are compared with the macroscale adhesion characterization results of fabricated microfibers to improve our understanding of the mechanics of microfibrillar adhesive interfaces. Moreover, there is no previous report of fabrication techniques for controlled angled fibers or testing of angled fibers similar to those seen in biological fibrillar adhesives. Detailed optical microscope images, mechanical behavior, and adhesion of micrrometer-scale fiber array interfaces during loading and unloading are shown in detail for the first time. Polyurethane microfibers (17−25 μm diameter) with different hardness, angle, and aspect ratio are fabricated using an ultraviolet (UV) lithography and polymer micromolding fabrication technique and tested with a custom tensile macroscale adhesion measurement setup. Here, micrometer-scale fibers are selected because they allow consistent fabrication results and they are large enough to be easily visible with optical microscopy. However, proposed theoretical models and fiber fabrication technique in this paper can be directly applied and extended to few micrometer or nanoscale fibers. Adhesion and overall work of adhesion of the microfiber arrays are measured and compared with the models to observe the effect of fiber geometry and preload.

In this paper, section 2 describes the modeling of microfibrillar adhesion and overall work of adhesion for single and arrays of polymer fibers. Next, fabrication of arrays of vertical and angled microfibers is described in section 3. Macroscale adhesion of the polymer microfibers is characterized using a custom tensile adhesion measurement setup described in section 4 along with the experimental results. The adhesion experiment results and their comparison with the analytical models and design optimization are discussed in section 5. Finally, conclusions and future directions are reported in section 6.

2. Modeling

An approximate analytical model for fiber adhesion is developed by combining the basic principles of elastic beam theory, surface interaction forces, and contact mechanics and applying them to high aspect ratio vertical and angled microfibers. The results from this model are compared to the adhesion experiments to determine the accuracy of the model and understand the adhesion mechanism of microfiber−surface interfaces in more depth.

2.1. Single Fiber Analysis. The procedure for finding the adhesive properties of an array of fibers starts with single fiber analysis as follows. First, flat punch theory is used to find the average adhesion strength of a single fiber. Next, beam mechanics is used to find the tensile stresses at the interface during loading. The pull-off force is determined by equating an "average tensile

(27) Tang, T.; Hui, C. Y.; Glassmaker, N. J. Can a fibrillar interface be stronger and tougher than a non-fibrillar one? *J. R. Soc. Interface* **2005**, *2* (5), 505−516.
(28) Yurdumakan, B.; Raravikar, N. R.; Ajayanb, P. M.; Dhinojwala, A. Synthetic gecko foot-hairs from multiwalled carbon nanotubes. *Chem. Commun.* **2005**, 3799−3801.
(29) Zhao, Y.; Tong, T.; Delzeit, L.; Kashani, A.; Meyyappan, M.; Majumdar, A. Interfacial energy and strength of multiwalled-carbon-nanotube-based dry adhesive. *J. Vac. Sci. Technol., B: Microelectron. Nanometer Struct.—Process., Meas., Phenom.* **2006**, *24*, 331−335.

stress" to the average adhesion strength. Finally, the pull-off force is related to fiber deflection through linear elastic beam equations. In reality, the pull-off is a complex process due to the singular stresses and nonlinearities at the fiber−surface interface. However, in our model, the criteria for pull-off are derived using the moments, forces, and stresses at the interface through a simplified linear model. This approximate linear model may not lead to the exact solutions but should describe the general trends in adhesion performance when varying the design parameters, and could therefore be useful in developing a fibrillar adhesive design methodology.

The fiber geometry is taken as a cylindrical beam with a flat tip which closely approximates the fabricated fibers discussed in section 3. Assuming the fiber contacts a locally flat surface, the adhesion (P_f) for a circular flat punch and a flat surface interaction is given as[19]

$$P_f = \sqrt{6\pi a^3 K w_f} \qquad (1)$$

$$K = \frac{4}{3}\left(\frac{1 - v_s^2}{E_s} + \frac{1 - v_f^2}{E_f}\right)^{-1} \qquad (2)$$

where w_f is the effective work of adhesion, a is the fiber radius, and K is the effective Young's modulus. E_s and E_f are the Young's moduli and v_s and v_f are the Poisson's ratios of the surface and the fiber material, respectively. Although eq 1 is derived from a rigid punch on an elastic soft surface, it is also a good first-order approximation for an elastic punch, which is softer than the flat surface,[2] as is the case for the polymer microfibers discussed in this work.

Using the pull-off force of a circular flat punch, the average adhesion strength (σ_c) can be determined as

$$\sigma_c = \frac{P_f}{\pi a^2} \qquad (3)$$

The pull-off of a single fiber is said to be flaw-insensitive[13] if the pull-off is controlled by the adhesive properties of the interface rather than the crack propagation. This condition is satisfied when the radius of the fiber (a) is less than a critical length d_c = $6Kw_f/(\pi\sigma_o^2)$[18] where σ_o is the intrinsic adhesion strength. This is an important condition for strong adhesion because the fiber tip is not guaranteed to be perfectly smooth and flat, and any defects could introduce cracks at the interface. With the values appropriate for the materials in our experiments (K = 5.2 MPa, w_f = 93 mJ/m², and σ_o = 0.1 MPa[27]), the critical length is calculated as $d_c \simeq 100$ μm, which is larger than the fiber radius, a = 12.5 μm.

To determine the pull-off force for the fiber−surface interface, the fiber is modeled as a fixed-guided cylindrical beam. The fixed boundary condition occurs at the end of the fiber that is affixed to the backing layer, and the fiber is assumed not to rotate or move at this end. The other end of the fiber, which is referred to as the tip of the fiber, is adhered to a surface and is assumed to have guided boundary condition, meaning that the fiber tip moves only in the direction normal to the backing layer (n-direction) and the undeformed angle at the tip is maintained (Figure 1b). With reference to Figure 1, the moment (M_x) is found from the rotation constraint at the fiber tip as
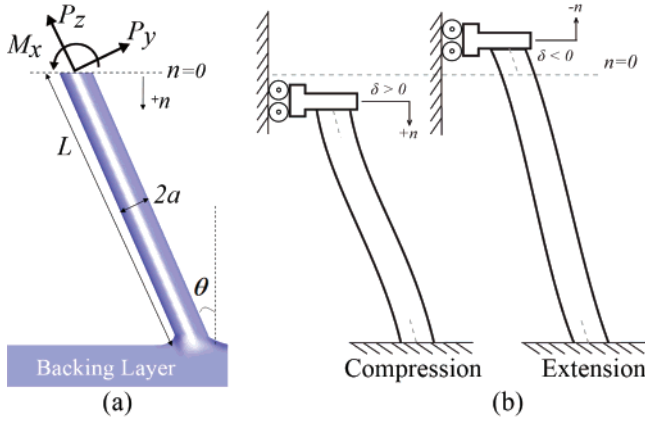
$$M_x = \frac{P_y L}{2} \qquad (4)$$

where L is the length of the fiber. The force exerted on the fiber

Figure 1. (a) Schematic of the forces on the tip of a single fiber. (b) Illustration of the fixed-guided boundary conditions of a fiber in contact with a locally flat surface during compression and extension. The angle of the fiber at both ends remains fixed, while the tip moves only in the n direction.

tip in y-direction (P_y) is related to the resultant force in the n-direction through $P_y = P_n \sin \theta$ where θ is the fiber angle. M_x introduces a normal stress at the fiber tip which is compressive for one-half of the tip and is tensile for the other half. In addition, the force in the z-direction $P_z = P_n \cos \theta$ creates a uniform tensile stress on the entire tip. Thus, the average stress on the half of the fiber tip (σ_{av}) where the moment M_x causes a tensile stress is

$$\sigma_{av} = c \left(\frac{P_n \cos \theta}{\pi a^2} + \frac{8 P_n L \sin \theta}{3 \pi^2 a^3} \right) \quad (5)$$

where c is the stress transformation factor. Since the tip of the fiber is not perpendicular to the axis of the fiber, the stress needs to be transformed to the tip plane, and for this specific case, $c = \cos^2 \theta$. For angled fibers, the pull-off force (P_{cf}) is chosen to be the force in the n-direction (P_n) that causes the average tensile stress (σ_{av}) to reach the average adhesion strength (σ_c). Thus, by replacing P_n with P_{cf} and σ_{av} with σ_c, eq 5 can be rewritten to obtain the pull-off force (P_{cf}) as

$$P_{cf} = \frac{3 \pi^2 a^3 \sigma_c}{(\cos^2 \theta)(3 \pi a \cos \theta + 8 L \sin \theta)} \quad (6)$$

Note from eqs 3 and 6 that, when $\theta = 0°$, $P_{cf} = P_f$, which is the pull-off force for vertical fibers. With the detachment criteria for a single fiber determined, it is possible to relate the deflection of the single fiber to the force it exerts on the surface through stiffness. This is an essential step to be able to expand the single fiber adhesion to the adhesion of fiber array. Each fiber is assumed to be an independent linear spring with stiffness in the loading direction derived using the following assumptions: (1) The fiber is a cylindrical beam which undergoes small deflections; (2) boundary conditions are fixed-guided; (3) the fiber tip is constrained to move only in the n-direction; (4) there is no shear at the interface; (5) the fibers are mechanically uncoupled.

The axial stiffness (k_z) and bending stiffness (k_y) of a fiber in Figure 1 can be defined as

$$k_z = \frac{\pi a^2 E_f}{L} \quad (7)$$

$$k_y = \frac{3 \pi a^4 E_f}{L^3} \quad (8)$$

If the fiber has an angle θ with respect to the n-direction (Figure 1), then the stiffness in the loading direction (k_n) is a combination of k_z and k_y[10] where

$$k_n = \frac{k_z k_y}{k_y \cos^2 \theta + k_z \sin^2 \theta} \quad (9)$$

It can be concluded from eqs 7−9 that, as the aspect ratio ($L/2a$) and the angle (θ) become larger, the fiber becomes more compliant. The effect of compliance will be analyzed in the latter sections, as it is an important factor in fiber array adhesion. With the stiffness (k_n) determined, the force (P_n) that the fiber applies to the contacting surface under a given deflection (δ_n) can be found simply by using the linear spring model as

$$P_n = k_n \delta_n \quad (10)$$

Note that P_n is positive when the fiber is under compression and is negative when the fiber is under tension. For the case where the fiber is under compression, buckling instability occurs after a critical buckling force (P_{cr}) is reached. The critical buckling force can be calculated using Euler's buckling formula for fixed-guided boundary conditions as

$$P_{cr} = \frac{\pi^3 E_f a^4}{L^2} \quad (11)$$

Here, the critical deflection δ_{cr} after which buckling occurs is given by

$$\delta_{cr} = \frac{P_{cr}}{k_z} \quad (12)$$

When buckling occurs, meaning $\delta_n = \delta_{cr}/\cos \theta$, the repulsive force for a single fiber becomes $P_n = P_{cr}/\cos \theta$. When the fiber is under tension, the maximum deflection (stretching) a fiber can experience before pull-off (δ_e) is limited by the fiber adhesion such that

$$\delta_e = \frac{P_{cf}}{k_n} \quad (13)$$

As the fiber stretches as a result of the adhesion, the deflection becomes $\delta_n = -\delta_e$, after which the fiber detaches from the surface and it has no net contribution to the overall adhesion ($P_n = 0$). The relation between the deflection of the fiber and the force the fiber exerts on a surface in contact can be summarized as follows:

$$P_n = \begin{cases} k_n \delta_n & -\delta_e \leq \delta_n < (\delta_{cr}/\cos \theta) & \text{(compressed or stretched)} \\ P_{cr}/\cos \theta & \delta_n \geq (\delta_{cr}/\cos \theta) & \text{(buckled)} \\ 0 & \text{otherwise} & \text{(detached)} \end{cases} \quad (14)$$

As mentioned earlier, the energy to separate bodies in contact, which can also be expressed in terms of stiffness and deflection, is another parameter that is critical to characterize the adhesive properties of an interface. Every fiber that contacts the surface will stretch a distance of δ_e before detaching. During this process, energy is not only lost through breaking of the fiber−surface interface, but is also lost through the stretching of the fiber. Thus, the overall energy (u_d) required to

separate a fiber from the surface becomes[13]

$$u_d = w_f \pi a^2 + \frac{1}{2} k_n \delta_e^2 \qquad (15)$$

2.2. Adhesion of an Array of Fibers. The adherence of a single fiber is determined using eq 1; however, determining the adherence of an array of fibers is not simply the product of the number of fibers in the array and the single fiber adherence. Fiber array adhesion is a function of many parameters such as fiber geometry, fiber spacing, and surface topography of the adhering surface. By knowing the value of these parameters, it is possible to expand the single fiber model from the previous section to evaluate the adhesive behavior of an array of fibers where each fiber has a deflection which is a function of the surface topography and the relative displacement (Δ) between the surfaces. By summing the contribution of each independent individual fiber in contact with the surface, the overall behavior of the array is determined. Clearly, in order to have a high overall force, the number of fibers in a given area should be maximized. However, there is a physical limit in fiber density, since the fibers may adhere to each other and not return to their upright positions. This coherence is known as lateral collapse, and the lateral stability condition for two cylindrical fibers is given by[10]

$$\left(\frac{\pi^4 E_f^* a}{2^{11} \gamma_f} \right)^{1/12} \left(\frac{3 E_f a^3 d^2}{\gamma_f} \right)^{1/4} > L \qquad (16)$$

where γ_f is the fiber material surface energy, d is the edge to edge distance between the fibers, and $E_f^* = E_f/(1 - \nu_f^2)$.

In order to determine the adhesion of an array of fibers, it is necessary to define the parameters of the contacting surface. The generalized surface will have parameters of surface energy, roughness, amplitude, and frequency. The roughness of the surface determines the height distribution, which will affect the deflection of the fibers in contact. For this analysis, the surface roughness wavelength is assumed to be much larger than the fiber radius so that flat punch tip assumptions from the single fiber analysis apply.

In an adhesion experiment, the adhering surface is brought into contact with the fiber array and pressed toward the fiber array with a compressive force referred to as preload P_p, which is reached at the maximum relative displacement (Δ_p) between the surfaces. $\Delta = 0$ when the first contact occurs. After P_p is reached, the adhering surface is retracted until the two surfaces fully separate. During retraction, the magnitude of the maximum tensile force is called adhesion (P_a). In such an adhesion experiment, the overall energy dissipated per unit area during the approach and separation process (W_t) is then a function of the energy per fiber (u_d), the number of fibers in contact at the preload (N_{max}), and the projected contact area (A_{max}) at the maximum relative displacement (Δ_p) as

$$W_t = \frac{N_{max} u_d}{A_{max}} \qquad (17)$$

One should note that, for a soft backing layer, the relative displacement not only causes the fibers to deform, but it may also deform the backing layer. Although we model each fiber as mechanically independent, the backing layer deformation is modeled using Hertz theory[18] and taken into account when determining the maximum contact area (A_{max}) and the number of fibers in contact at this point (N_{max}).
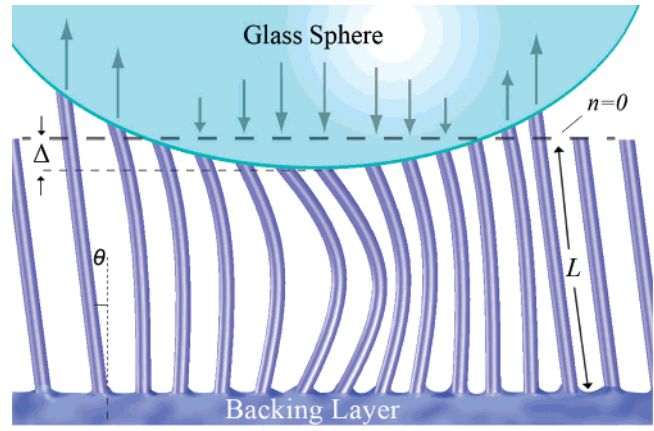
Figure 2. Schematic of a sphere retracting from an array of fibers (not to scale). The fibers close to the middle of the sphere are compressed, and the ones that are in contact on the edges are stretched. The arrows in the diagram represent the direction and relative magnitude of the forces on the fibers.

Table 1. Sample Geometry for Experimentally Tested Short and Long Vertical and Long Angled Fibers

sample type	height	diameter (2a)	length (L)	angle (θ)	fiber spacing (d)
short vertical	48 μm	20 μm	48 μm	0°	40 μm
long vertical	100 μm	25 μm	100 μm	0°	40 μm
long angled	75 μm	25 μm	79 μm	18°	40 μm

After the preload is applied, in the process of separation, for any given displacement of the rough surface relative to the fibrillar surface, it is possible to determine the deflection of each fiber and therefore the force each fiber exerts on the surface. The resulting force is a function of the relative displacement (Δ), surface roughness, and the fiber array geometry (fiber spacing, length, and radius).

Using eq 14, the sum of the forces that each fiber contributes, adhesion for fibers in tension and repulsion for fibers in compression (Figure 2), gives us the overall force (P) exerted by the fibrillar surface as

$$P = \sum_{i=1}^{N} P_{n,i} \qquad (18)$$

$P_{n,i}$ is the force contribution of the ith fiber, which is dependent on its individual deflection ($\delta_{n,i}$), and N is the number of fibers in contact at a given displacement. During separation, the minimum value of P is the maximum separation force (P_a). The adhesion pressure (p_a) is defined following the derivation of maximum separation force as

$$p_a = \frac{P_a}{A_{max}} \qquad (19)$$

The model is implemented in *MATLAB* to simulate the adhesion of fiber arrays detailed in Table 1. The geometry of fibers in Table 1 is determined from the optical microscope images of the fibers usind in the experiments. Material properties of polyurethane fibers used for the simulations are $E_f = 5.2$ MPa, $w_f = 93$ mJ/m^2, and $\nu = 0.5$. E_f and w_f are experimentally determined as described in the following sections.

The surface used in the experiments and simulations is a hemisphere (Figure 2), because a hemisphere represents a special case of a rough surface with a well-defined height distribution which is immune to alignment and orientation issues. The simulation results are then compared to the experimental results
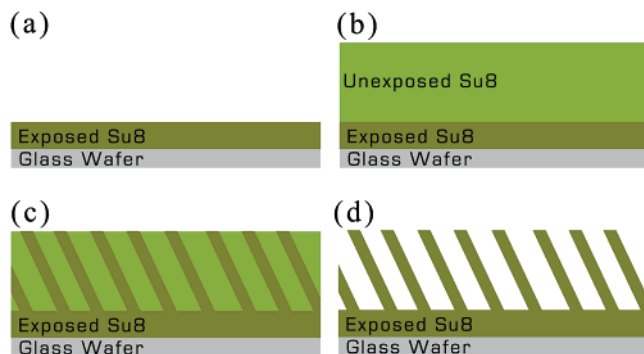
Figure 3. Process steps of the polymer microfiber fabrication: (a) A thin layer of SU-8 is spun on a glass substrate then exposed and cured; (b) a thicker layer of SU-8 is spun which will become the fibers; (c) the thick layer is patterned with UV exposure; (d) the SU-8 photoresist is developed, leaving the desired fiber array.

in section 4.1, and the model is extended to simulate the adhesion behavior for different fiber materials and geometries in section 5. Here, the radius of the sphere $R = 6$ mm is chosen to be much larger than the radius of the fiber a, so that the flat punch assumption in eq 1 applies.

3. Microfiber Fabrication

Polymer microfiber arrays are fabricated through a micro-molding process which duplicates lithographically formed master template structures with a desired fiber material. This technique enables fabrication of fiber array patches on up to an 8 in wafer inexpensively and with high yields. This is a significant advantage in comparison to other proposed fibrillar adhesive fabrication techniques.[9,21,29] Also, this method allows for design and fabrication of fibers with nonvertical orientation. The fabrication details are described below.

3.1. Master Template Fabrication. The master template for the molding process is fabricated from SU-8 photoresist (SU-8 2025, MicroChem) on a glass wafer substrate. A glass wafer is used to prevent UV reflections during angled lithography. First, a thin layer of diluted SU-8 polymer is spun onto a substrate wafer to provide a thin polymer backing for the microfibers. The layer is baked and uniformly exposed to UV light (Figure 3a). This backing layer was found to be crucial for the process, since the adherence between SU-8 and substrate is too weak to keep the high aspect ratio microfibers anchored firmly otherwise. Next, another layer of SU-8 is spun atop the first layer as seen in Figure 3b. The thickness of this layer determines the height of the microfibers, usually between 30 and 100 μm. A contact mask with 2 to 20 μm diameter circular clear areas in square packing arrangement is used to pattern the wafer with directional UV light (Figure 3c). The wafer is then developed in a liquid bath (SU-8 developer, MicroChem) for up to 20 min to remove the unexposed photoresist, leaving the pattern of exposed polymer pillars (Figure 3d).

For initial fabrication, the exposure was perpendicular to the surface to form vertically oriented fibers. Results from this lithographic technique can be seen in Figure 4a. Large arrays on the order of 300 mm² of long hairlike independent fibers are produced. Fibers with diameters from 4 to 25 μm are produced with aspect ratios of up to 20:1. Fiber arrays of 10:1 aspect ratio exhibit excellent uniformity and tend to remain upright.

UV diffraction and the SU-8 properties limit the resolution to approximately 2 μm for high aspect ratio structures, and consistent fabrication of features of this size is challenging. More advanced exposure techniques may be employed to reach higher aspect ratios or smaller diameters. For example, Bogdanov et al. have demonstrated using X-ray lithography that it is possible to form
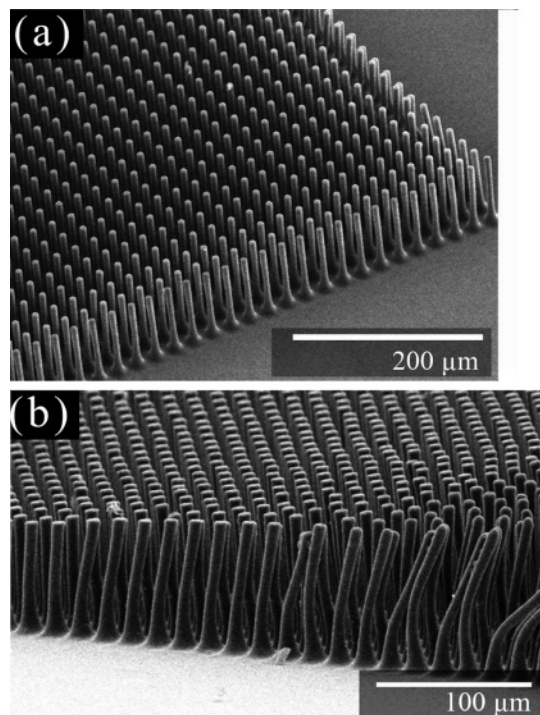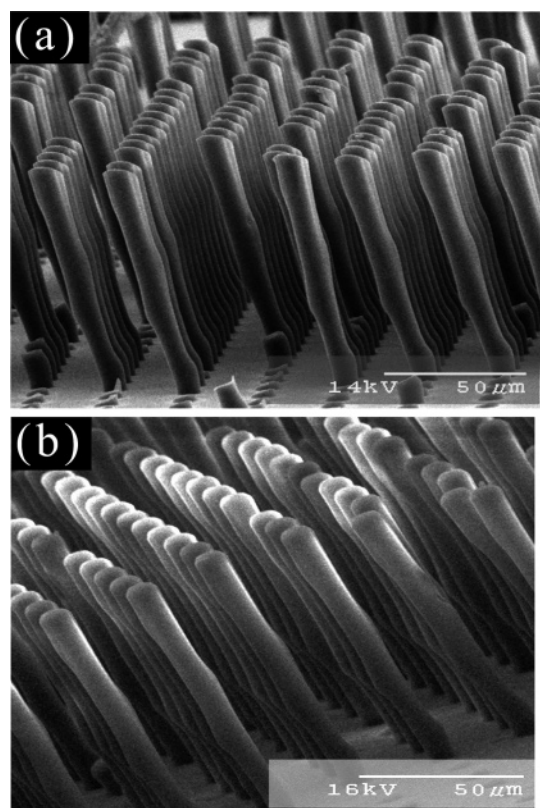

Figure 4. (a) SEM micrograph of 6 μm diameter SU-8 polymer high aspect ratio fiber array. (b) As fiber length increases (from left to right) past the maximum stable length, the fibers collapse together.

vertical independent SU-8 fibers with aspect ratios in excess of 50:1.[5] X-ray lithography also allows for submicrometer diameter features[24] which can be used for nanofiber fabrication.

To avoid fiber clumping, the geometry parameters for the fibers are selected by considering the energy balance equation given by eq 16. The lithography mask determines the radius and spacing between fibers, leaving only fiber length and angle as variables. Fiber length is determined by the thickness of the SU-8 layer and can be varied by changing the SU-8 viscosity or spin speed.

Collapse occurs during the drying phase after development and rinsing when water droplets repel the hydrophobic fibers, pressing them into contact with each other. The dependence of collapse on fiber length can be seen in Figure 4b where the only variation across the image is increasing fiber length from left to right. The shorter fibers on the left side are standing independently alongside the longer fibers which have collapsed laterally. Collapse generally occurs between more than a pair of fibers, so in addition to the distance between adjacent fibers, the arrangement pattern of the fibers determine clumping conditions. Square packing of fibers has been determined to allow close packing without clumping.[17]

Angled microfibers are fabricated using the same lithographic technique. Simply by varying the UV exposure angle by tilting the wafer during exposure, the fibers are formed at a nonper-pendicular angle to the substrate surface (Figure 5a). Using Snell's law, the UV exposure angle can be calculated for the desired fiber angle.[14] From our tests, tilting the wafer with around a 45° slope reliably formed fibers with angles of around 25° from vertical. Hung et al. showed that angled structures of up to 60° from vertical are achievable by immersing the wafer in glycerol during exposure to decrease refraction.[14] One advantage of this method for fabricating angled fibers is that the tip shape is flat and roughly parallel to the substrate rather than perpendicular to the fiber axis. This increases the contact area of the tips when in contact with a surface.

Figure 5. (a) SEM micrograph of 8 μm diameter SU-8 high aspect ratio angled fiber array master template. (b) Polyurethane molded microfibers with the same geometry.

3.2. Micromolding. Since the SU-8 material properties are not ideal for use as a structural material due to its brittleness and weak bond with the backing substrate, it is desirable to create a mold in which to replicate the fibers with a different polymer material. Moreover, molding enables the selection of wide range of polymer materials as the fiber material, and the master template can be used tens or hundreds of times, which increases the fabrication speed and reduces the cost significantly. A compliant mold is fabricated by pouring a liquid silicone rubber (HS-II, Dow Corning) over the wafer and allowing it to cure at room temperature for 24 h. Once cured, the mold is carefully peeled away from the template wafer, resulting in a flexible mold with the negative shape of the SU-8 fibers. This mold is used to vacuum-mold liquid polyurethanes or other curable materials (except silicone rubbers which bond to the template rubber material) with the desired physical properties. Once cured and demolded, the polyurethane fibers have roughly the same geometry as the original SU-8 fibers.

Using this method, the microfiber material may be altered to suit the intended design. However, the same lateral collapse laws apply, so the design must stay within the lateral collapse requirements for both SU-8 (to create the template) and the secondary fiber material to ensure that self-supporting independent fibers are formed. This technique has been successfully implemented to create angled high aspect ratio polyurethane fibers from SU-8 master arrays (Figure 5). However, the successful demolding of high aspect ratio SU-8 fiber arrays without fracturing many of the fibers is a significant challenge.

4. Macroscale Adhesion Experiments

Fiber array test samples were fabricated using the methods described in section 3 with polyurethane elastomers (ST-1087 and ST-1060; BJB Enterprises) which have high tensile strength

(6 MPa) and are available commercially with a wide range of elastic moduli. The hardness of these polymers are Shore 83A and 60A, respectively, and were determined through tensile testing to have Young's modulus of approximately 9.8 and 2.9 MPa, respectively. Fiber arrays with varied lengths and angles were fabricated for testing as described in Table 1. These geometries were selected because they allow consistent fabrication results and are large enough to be easily visible with optical microscopy. The backing layer is approximately 2.5 mm thick for all samples.

First, an atomic force microscope (AFM) (Veeco CP-II) is used to characterize the polyurethane−glass interfacial effective work of adhesion w_f, which is used to calculate the adherence of a single fiber in eq 1. In contrast to the data from macroscale measurements of a flat polyurethane sample, the AFM data exhibit reduced bulk viscoelastic effects and more closely approximate the single fiber adhesion. In the absence of bulk viscoelastic effects, the surface viscoelastic losses and the thermodynamic work of adhesion can be combined into a single term, w_f, which is used in elastic theory equations[31] to predict the adhesion of a single fiber. A 12 μm diameter silica particle attached AFM probe (Novascan) with 14 N/m bending stiffness is used to measure the pull-off force between the particle and a flat polyurethane surface using ten measurements. Using the Johnson−Kendall−Robert (JKR) adhesion model for a sphere−plane interaction, w_f is computed from[16]

$$P_{cs} = \frac{3}{2} \pi R_p w_f \tag{20}$$

where P_{cs} is the pull-off force and R_p is the particle radius. Using the measured pull-off force and eq 20, the effective work of adhesion w_f for glass and ST-1060 polyurethane interface was computed to be 93 mJ/m^2.

In most of the previous works,[9,28] micro/nanoscale local adhesion of synthetic fibers was tested using an AFM. Although these local measurements can give detailed insight into the individual fiber adhesion micro/nanomechanics, the overall macroscale behavior of the fiber array can be significantly different. Moreover, AFM-based or other[21,29] local measurements do not allow observation of the fiber tip contact during the adhesion measurements. Therefore, macroscale adhesion and overall work of adhesion of fabricated polymer microfiber arrays are characterized in this work using a custom tensile adhesion measurement setup with an optical imaging capability to observe the real-time contact area.

The custom macroscale adhesion measurement system consists of a top-view reflection type optical microscope (Nikon Eclipse L200) or an inverted optical microscope (Nikon Eclipse TE200) with an automated high precision stage (MFA-CC; Newport) which holds a high-resolution load cell (GSO-25; Transducer Techniques, Inc.). A 12 mm diameter glass hemisphere (QU-HS-12; ISP Optics) is connected to the load cell. The adhesive samples are placed on the microscope stage with the fiber arrays facing toward the glass hemisphere. Custom real-time software controls the stage to move the hemisphere into contact with the fiber sample at a fixed velocity until a prespecified preload force is reached. The hemisphere is then retracted at a speed of 1 μm/s until it detaches from the sample. The software continually captures the force data from the load cell as well as time-stamped video from the microscope.

(30) Haiat, G.; Phan Huy, M. C.; Barthel, E. The adhesive contact of viscoelastic spheres. *J. Mech. Phys. Solids* **2003**, *51*, 69−99.
(31) Shull, K. R. Contact mechanics and the adhesion of soft solids. *Mater. Sci. Eng., R:* **2002**, *36*, 1−45.
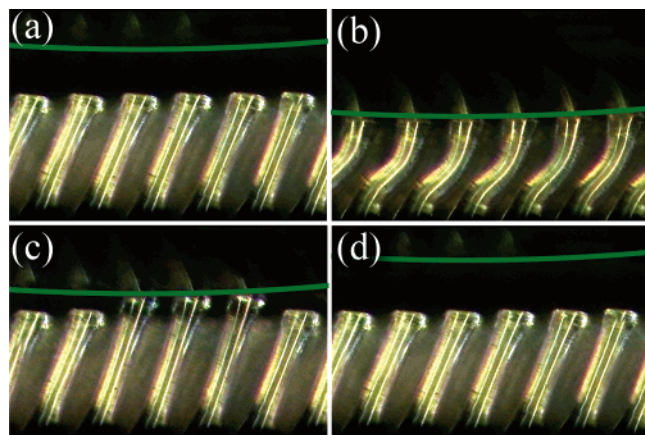
Figure 6. Optical microscope profile view image frames from a typical measurement showing 25 μm diameter long angled ST-1060 polyurethane fibers with a line overlaid on the edge of the glass hemisphere for clarity: (a) before contact with the glass hemisphere, (b) fibers during compression without loss of tip contact, (c) fiber extension of the three last attached fibers, and (d) the fibers after contact is lost.

Two types of experiments are possible with this setup. The first mode, referred to as *profile view mode*, uses a cut cross section of the fiber array area which contacts only half of the hemisphere under the top-view microscope. This allows the camera to record images and video of the fiber deformation during contact and retraction. Using this setup mode, it is possible to observe the compression, bending, buckling, and stretching behavior of the fibers during the testing as seen in Figure 6. In the other mode, *inverted view mode*, the hemisphere contacts the center of the array of fibers. This mode provides more consistent adhesion data and allows viewing of the real contact area. Thus, profile view mode is used to examine the qualitative behavior of the surfaces during contact, whereas inverted view mode is used for quantitative analysis.

For computing the overall work of adhesion for the macroscale measurements on the fiber arrays, force−distance data from the hemisphere tests are used to calculate the energy dissipation U_d by numerically integrating the area between the loading and unloading force curves. The known deflection of the load cell stem is used to correct the displacement data before the area integration is realized. Corrected force−distance data from a single measurement is shown in Figure 7. In this case, an array of long vertical polyurethane fibers was tested with a 1 mm diameter steel sphere. The sphere starts above the fiber array tips (A). The force during the approach is zero until the sphere makes initial contact with the fibers at $n = 0$. The preload force (P_p) is the maximum positive force peak (B) when the sphere has penetrated the fiber array by distance Δ_p. The force equilibrium point (C) occurs when the tension in the outer fibers is balanced by the compression of the inner fibers. Note that point (C) and
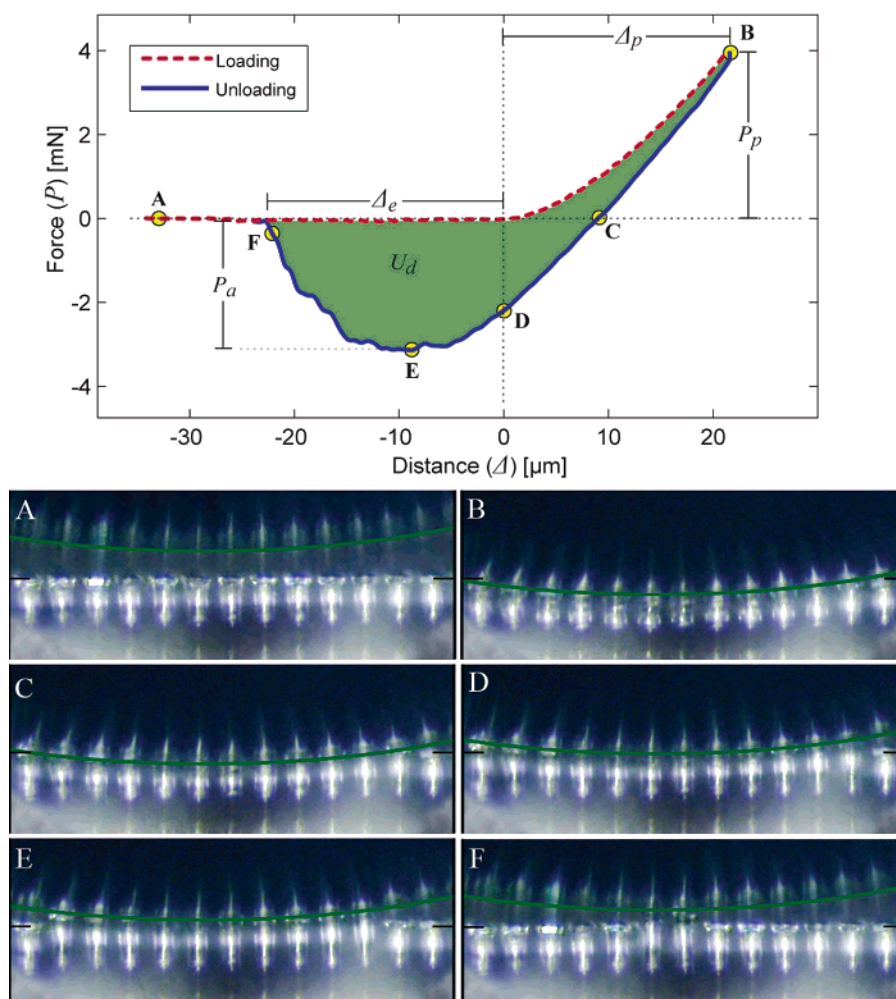
Figure 7. Sample force−distance experimental data during a typical profile view mode imaging of a manually cut cross section of long vertical ST-1060 polyurethane fibers. The images from the time-stamped video correspond to the labeled points in the force−distance curve and show the compression due to the preload force (point B) and extension during unloading (points C−F) with green lines overlaid on the edge of the hemisphere and black marks on $n = 0$ for clarity. Maximum separation force occurs at point E.
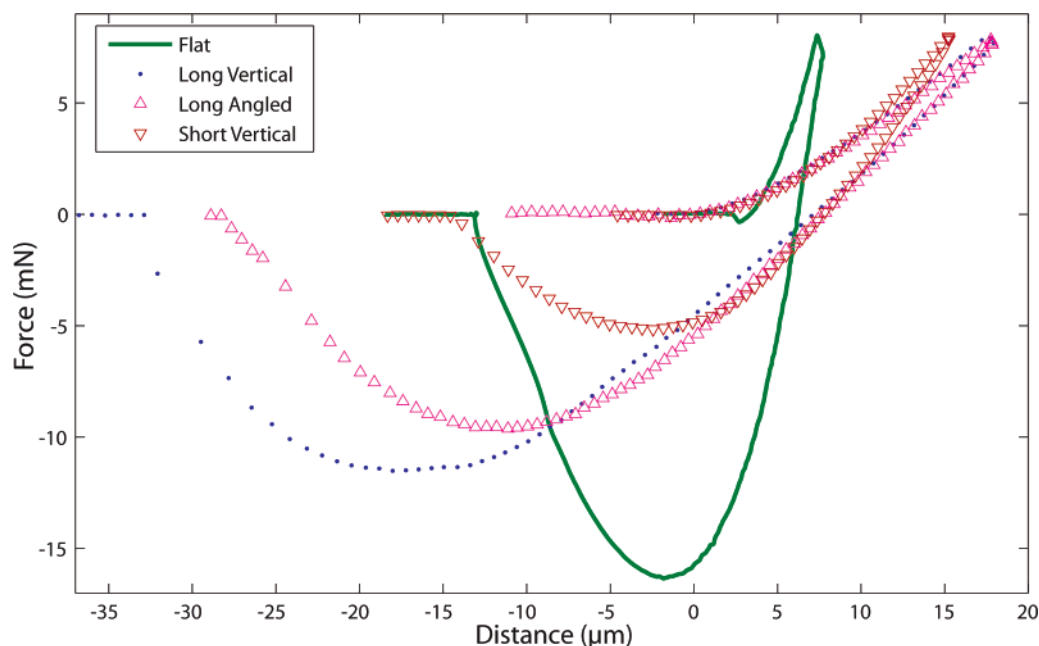
Figure 8. Force−distance plots for the tested flat, long and short vertical, and long angled fiber array samples given in Table 1. Each line is an average of data over three runs under identical conditions with 8 mN preload.

the corresponding image indicate this occurs before the sphere is completely retracted beyond the fiber tips. When $\Delta = 0$ (D), all of the contacting fibers are in tension. As the sphere continues to retract, the fibers extend, and the most highly extended fibers lose contact. The maximum separation force (P_a) is the value of the negative peak (E) where the sum of the forces of the contacting fibers is the greatest. After this point, the total force decreases, because the loss in adhesion due to fibers detaching is greater than the force due to the increased extension of the attached fibers. Finally, the last fiber is stretched (F) to its maximum ($\delta_e = \Delta_e$) and then pulls off, returning the overall force to zero.

4.1. Experimental Results. The initial results from experiments in profile view mode indicated that the stiffer ST-1087 polyurethane fibers lose tip contact when compressed, greatly reducing the contact area and adhesion. This was particularly problematic for angled fibers, which showed almost no extension or adhesion. The more compliant ST-1060 polyurethane fibers did not exhibit this behavior and remained in full contact when compressed, as seen in Figure 6b. Figure 6b also suggests that the fixed-guided boundary conditions used in the modeling section are appropriate. This resulted in the increased extension (Figure 6c) and adhesion of the softer fibers. Therefore, the remainder of experiments discussed in this paper were conducted on the more compliant ST-1060 polyurethane fibers.

A series of experiments were conducted in inverted view mode on a flat polyurethane control sample and the fiber arrays detailed in Table 1. The preload force was varied from 1 to 50 mN, and the approach and retraction speeds were 1 μm/s. Five measurements were taken for each sample at each of eight preselected preload values, and the contact point was moved to a different location on the fiber array for each measurement.

Averaged force−distance data from the experiments at 8 mN preload for all of the sample types are plotted together in Figure 8, which provides a visual comparison of the performance of the various samples. The flat sample shows the highest stiffness with least penetration depth (Δ_p) followed by the short vertical fibers, long vertical, and long angled fibers, respectively. The maximum separation force (P_a) is higher for the flat material than for any of the fiber samples. The flat sample has the smallest

maximum extension (Δ_e), followed by the short vertical, long angled, and long vertical fiber samples, respectively.

To examine the effect of preload on maximum separation force, a plot is generated from the maximum separation forces for each sample for the range of preload values (Figure 9a). The data are plotted along with the simulation results for the same fiber and hemisphere geometry. A similar plot is generated to examine the effect of preload on dissipated energy (Figure 9b). In the figure, the simulation results are the lines (LV, long vertical; LA, long angled; SV, short vertical), and the experimental data are the markers. All curves show an increase in adhesion with increased preload.

Although the preload values were controlled for each experiment, the contact areas are not consistent across the various samples because of their varying softness. In order to determine adhesion strength and overall work of adhesion trends, it is necessary to divide the total force or dissipated energy by the maximum contact area.

The relationship between preload force and real maximum contact area (A_{max}) was found using image processing methods. Contact areas were calculated for the same eight preload values for each sample using image subtraction methods on the corresponding video. To see A_{max} in a given frame, a reference frame with no contact is subtracted, leaving only the difference between the two images, which are the contacted fibers (Figure 10). The contact area is taken as the area of the smallest circle which contains all of the contacting fibers. These A_{max} values are used to calculate the adhesion strengths and overall work of adhesion (W_t). For the simulation data, the simulated maximum contact area is used. Preload pressure, adhesion strength, and work of adhesion are calculated by dividing the preload, maximum separation force, and energy dissipation (U_d) by A_{max}, respectively. The adhesion strength (p_a) and overall work of adhesion (W_t) values are plotted with respect to preload pressure in Figure 11.

5. Discussions

The purpose of the proposed model is to predict the trends and relative performance for fiber arrays. Since the contact mechanics for a compliant material in such an interface with forces and
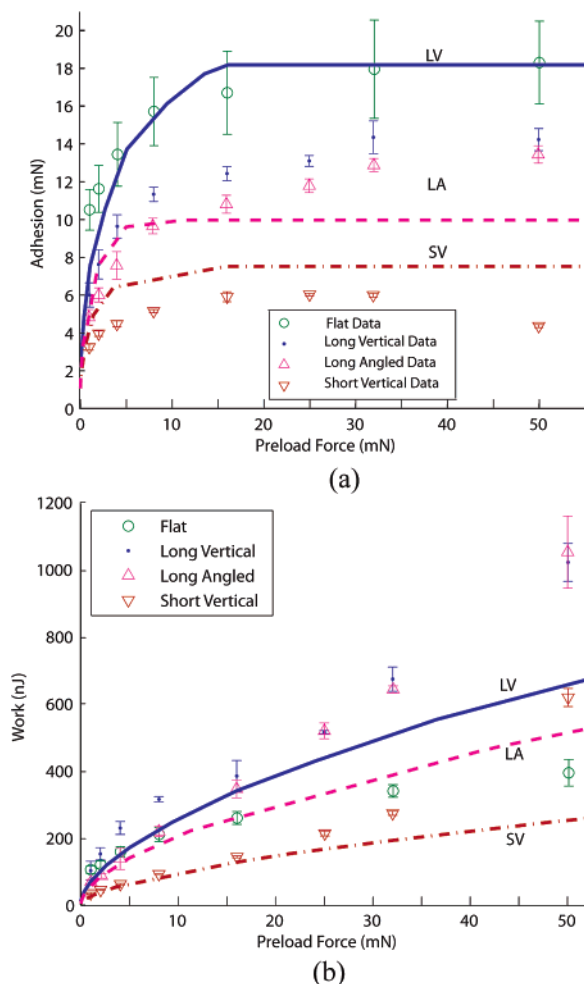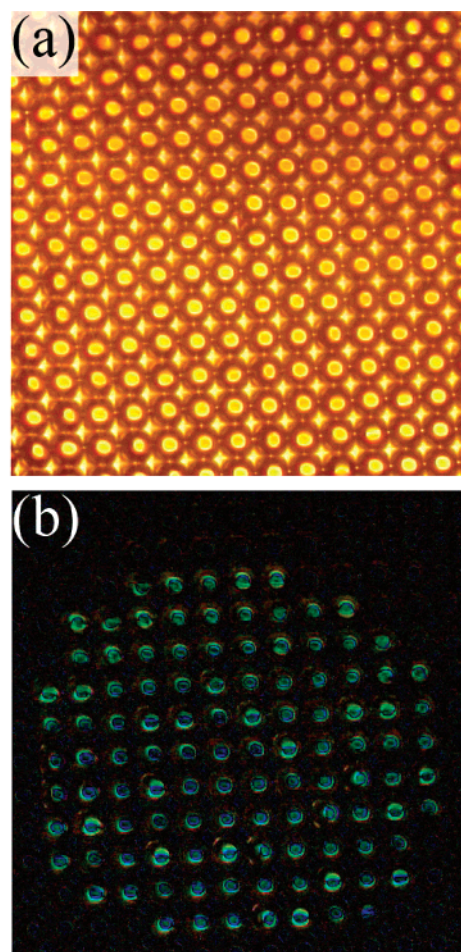
Figure 9. (a) Maximum separation force as a function of preload for the tested samples. (b) Energy dissipation as a function of preload. The simulation results are lines (LV, long vertical; LA, long angled; SV, short vertical), and the experimental data are markers.

Figure 10. (a) Inverted microscope image frames during testing 25 μm diameter long vertical fibers from below. (b) Real maximum contact area created from the same frame by image subtraction methods.

peeling torques are complex, the equations used to model this interaction in the simulation may be overly simplified, so we do not expect to predict the adhesion and work values with high accuracy. The results seen in Figure 9a demonstrate that, although the agreement between the experimental and predicted values is poor in some cases (e.g., long vertical sample), the model does predict the relative performance and trends for the fiber array samples tested.

An individual long vertical fiber has a lower stiffness value (k_n) but a similar pull-off force to a short vertical fiber. Therefore, a long vertical fiber can extend more, so that more fibers are in contact when the maximum adhesion occurs. According to the model, this increases the maximum adhesion of the fiber array. As the model predicts, the experiments show that the long vertical fiber array has higher adhesion than the short vertical fiber array.

The prediction of the effect of angle of the fibers on the fiber array adhesion performance is not as straightforward. Although the resulting pull-off force for angled fibers is lower due to the moment (M_x), angled fibers are more compliant and may exhibit larger deflections before detaching. In order for the fiber angle to improve the overall fiber array adhesion over that of the vertical fiber array, the higher number of attached fibers due to reduced stiffness must outweigh the lower adhesion force per fiber. For the specific fiber geometry in the experiments, this was not the case. The model correctly predicted that the decreased stiffness did not compensate for the decreased pull-off force due to the moment, leading to lower adhesion than the long vertical fiber

array. However, the increased extension did provide improved performance over the short vertical array. The same effects are seen in Figure 9b, as the dissipation energy is also a function of pull-off force and fiber extension and the trends in the experimental results agree with the model.

Angled fibers may lead to enhancement in adhesion when the surface roughness amplitude is high relative to the fiber length or when the fiber material has a high Young's modulus. In both of these cases, the dominant factor in adhesion is the number of fibers in contact at pull-off rather than the magnitude of the pull-off force of an individual fiber. One example where this situation is likely to occur is the use of carbon nanotube arrays as fiber adhesives.[29] Furthermore, submicrometer-scale diameter fiber tips can be more accurately approximated as a hemisphere than as a flat punch. This changes the guided boundary condition at the tip and allows rotation which removes the moment effect, eliminating the drawback of lower adhesion force per fiber completely. Finally, angled fibers would have a significant advantage due to their anisotropic friction behavior,[25] which would enhance the controlled attachment and detachment of the fibers.

Figure 11a also demonstrates an agreements between the modeled and experimental trends. In contrast to the adhesion force plot in Figure 9a, the adhesion strength of the long angled sample is lower than that of the short vertical sample. For the same applied preload, the maximum contact area A_{max} is higher for the long angled sample; as a result, the adhesion strength is lower.
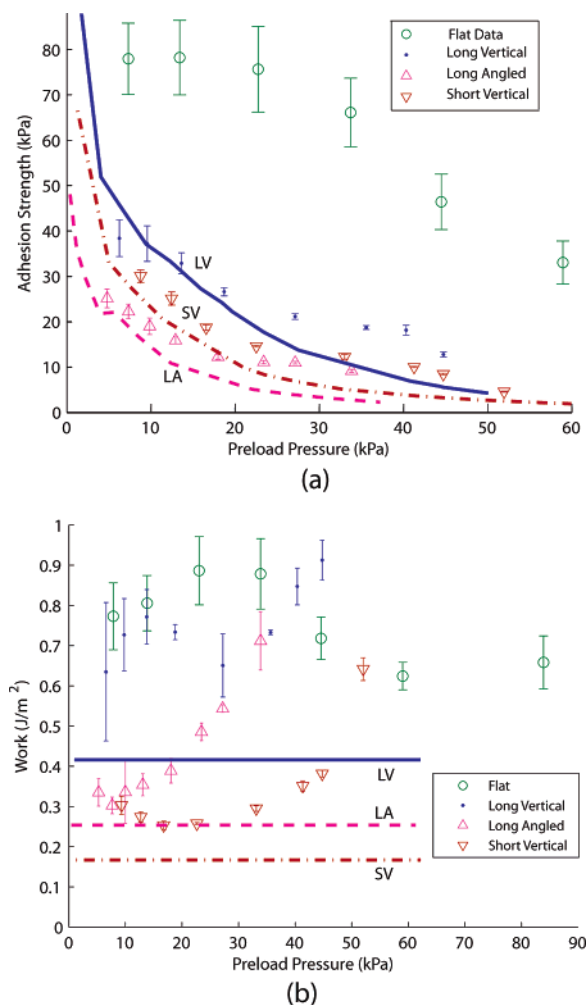
Figure 11. (a) Adhesion strength and (b) overall work of adhesion as a function of preload pressure. The simulation results are lines (LV, long vertical; LA, long angled; SV, short vertical), and the experimental data are markers.

Although the relative overall work of adhesion trend between the samples predicted by the model are in agreement with the experimental data, there is a significant discrepancy between the values (Figure 11b). There are many factors which may affect the agreement between the simulations and experimental data. First, the linear stiffness approximation is valid for small indentation depths and fiber extensions, but if the deflections are large, this assumption does not apply. For this reason, the simulated and experimental maximum contact areas diverge for large preloads, causing a larger discrepancy between experiments and simulations when the results are plotted with respect to preload pressure (Figure 11) than when plotted with respect to preload force (Figure 9). Also, the backing layer deformation observed was significant, up to 50% of the relative displacement for the relatively stiff short vertical fibers under the highest preloads. The linear superposition of the fiber deformation and the backing layer deformation using the Hertz model as incorporated in this work are not accurate, nor does the mechanical independence of the fibers assumption apply when such extreme deformations occur. This leads to disagreement in the overall work of adhesion results.

Also, the simulation assumes that the time scale for the retraction is comparable with the relaxation time of the fiber material, while in the experiments, this was not the case. For the viscoelastic polymer, the retraction speed, which is limited to 1

μm/s by the precision positioning stage and sensor drift, is not slow enough to prevent all viscoelastic effects.

From Figure 9a, the adhesion of the flat control sample is higher than that of all the fiber samples. This is likely due to the bulk and surface viscoelastic response of the material. Since JKR theory predicts that the adhesion of the flat sample should not change with preload, it is clear from Figure 9a that there are significant bulk and surface viscoelastic effects[30] which increase the adhesion of the flat control sample, particularly for high preloads. Unmodeled bulk viscoelastic effects resulted in significant discrepancies between overall work of adhesion theoretical models and experimental data in Figure 11b.

In addition, the beam bending equations are used to approximate the spring constants, and forces on the angled fibers are accurate only for beams of 10:1 length to thickness ratios or higher. These equations were applied to our angled fibers, which have an aspect ratio of approximately 4:1 leading to possibly inaccurate results. The simulation assumes perfect contact of all fibers and represents a theoretical maximum adhesion. In the tests, it is observed that fibers pull off stochastically. While the pull-off follows the general predicted trend, there is some randomness to the order in which fiber pull-off occurs.

5.1. Optimized Fiber Array Design. The fiber samples tested in section 4 were not optimized for performance and show little benefit over the flat fiber material. However, they do confirm that the numerical simulations predict the relative behavior of the fiber arrays, and therefore, the model can be used to investigate the performance of fiber arrays with varied geometry and material properties. The model from section 2.2 was extended to cover a wide range of diameters and lengths for a given fiber material and can be used to choose the optimum parameters for the fiber geometry and material for a given surface roughness. In contrast to the experiments from the previous section where the fiber spacing is fixed and constant across all samples, the simulations use the smallest fiber spacing allowed by eq 16, because this spacing allows for the highest possible adhesion.

As an example of how the simulations might be used to select the optimum fiber design geometry and material, in Figure 12, the adhesion strengths for the case of a 12 mm diameter hemisphere indenting 4 μm ($\Delta_p = 4 \mu$m) are plotted for varying fiber length and diameter and for two specific fiber angles and Young's modulus. This indentation depth correlates to a surface roughness of 4 μm amplitude with approximately 70 μm wavelength. The adhesion strength is found by dividing the adhesion by the projected area for the 4 μm indentation. The material properties that are held constant for all four plots are $\gamma_f = 14$ mJ/m^2, $w_f = 93$ mJ/m^2, and $\nu_f = 0.5$. The contour lines represent constant adhesion strengths.

The optimization plots indicate that stiffer materials improve the adhesion performance. For stiffer material, the optimum aspect ratio is higher and fiber diameter is smaller than for softer materials such as the polyurethane used in the experiments. However, the simulations assume perfect tip contact, which may not be possible for stiffer materials, and this may negate the apparent improvement in performance. These optimization plots also indicate that, for this set of parameters, vertical fibers have higher adhesion strengths than angled fibers. However, this is not necessarily the case for other fiber materials and surface roughness.

6. Conclusion

An approximate model was developed to predict the adhesive properties of arrays of microfibers based on fiber bending, compression, buckling, and extension in combination with contact mechanics. The model takes into account parameters such as
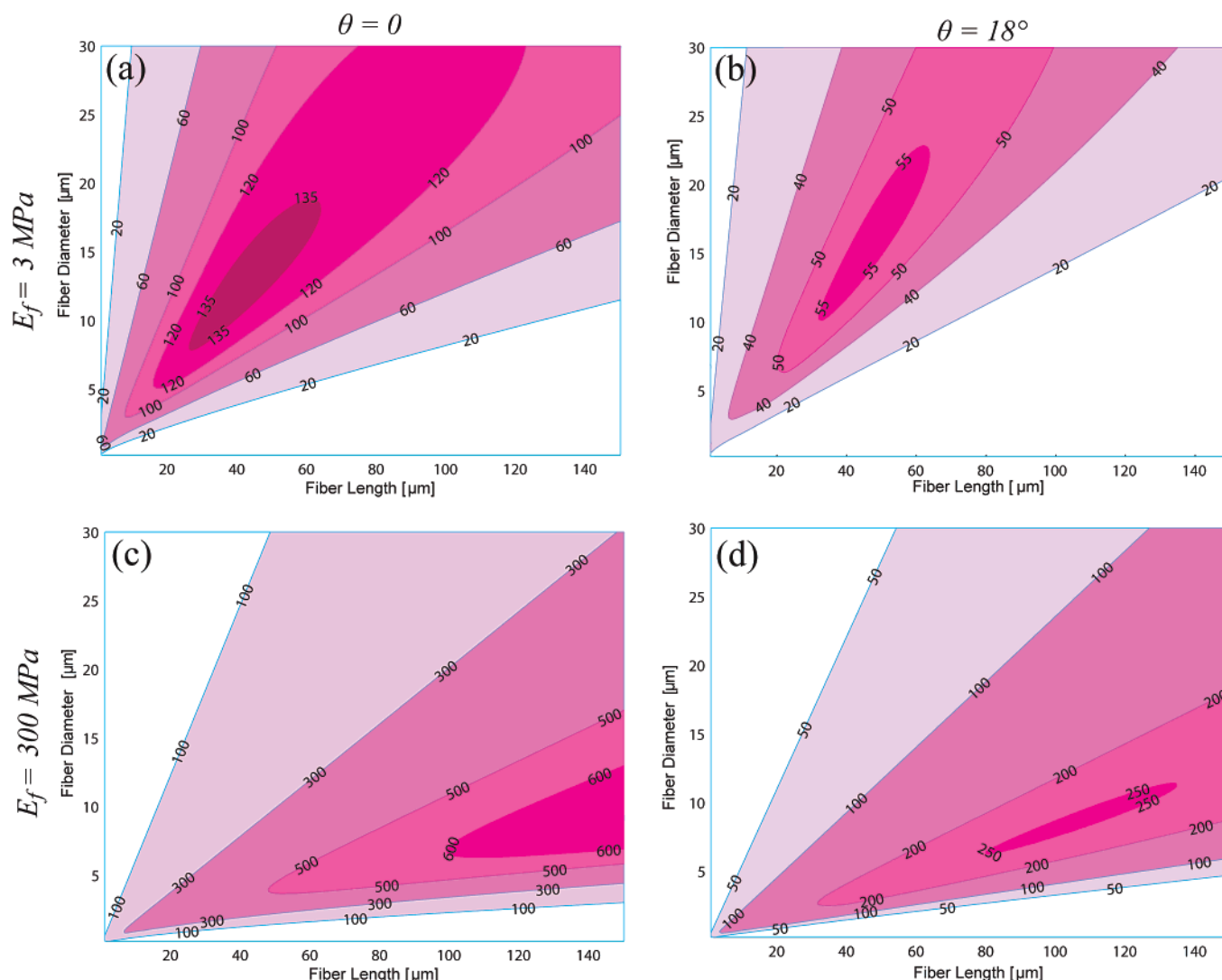
Figure 12. Example optimization plots for (a) $\theta = 0°$, $E_f = 3$ MPa; (b) $\theta = 18°$, $E_f = 3$ MPa; (c) $\theta = 0°$, $E_f = 300$ MPa; (d) $\theta = 18°$, $E_f = 300$ MPa. The figure is plotted for a 4 μm indentation depth with a 12 mm diameter glass hemisphere. The common material properties for all plots are $\gamma_f = 14$ mJ/m², $w_f = 93$ mJ/m², and $\nu_f = 0.5$. Each contour line represents a constant adhesion strength in kPa.

fiber material properties, fiber dimensions, fiber angle, and surface geometry. Also, the feasibility of fabricating high density and high aspect ratio microfiber arrays in large areas has been confirmed. The use of UV photolithography as a fabrication process for high aspect ratio self-supporting microfibers has been demonstrated, including fabrication of angled fiber arrays. Micromolding high aspect ratio angled polymer microfiber arrays by means of a compliant intermediate mold was demonstrated. Fabricated microfiber array samples were tested using a custom adhesion measurement system, and the results were compared with theory. The simulation results were found to predict the macroscale adhesive behavior trends of the microfiber arrays. A scheme was developed to aid in optimal fiber adhesive design and to examine the effect of fiber and surface parameters.

Future work includes generalizing the model incorporating various roughness distributions, more accurate backing layer deformation, and a more complex fiber tip shapes, such as fibers with spatular tips.[32] Fabrication techniques will be refined to allow fabrication of fibers with spatular tips and smaller-sized fibers for improved fibrillar adhesives and comparison with the model to confirm its validity at different size scales.

(32) Kim, S.; Sitti, M. Biologically Inspired Polymer Microfibers with Spatulate Tips as Dry Fibrillar Adhesives. *Appl. Phys. Lett.* **2006**, *89*(26), 26911−26913.